Hybrid Acoustic Noise Analysis Approach of Conventional and Mutually Coupled Switched Reluctance Motors

Jianning Dong, *Member, IEEE,* James Weisheng Jiang *Member, IEEE,* Brock Howey, Haoding Li, Berker Bilgin, *Member, IEEE,* Alan Callegaro and Ali Emadi, *Fellow, IEEE*

Abstract—This paper presents a method to calculate the acoustic noise of conventional switched reluctance motor (CSRM) and mutually coupled switched reluctance motor (MCSRM). This method is based on dynamic electromagnetic models, combined with analytical estimation of the stator eigen-modes and radiation efficiency, considering the switching effects and frame effects. The proposed method is applied to predict and compare the acoustic noise performances of a CSRM and an MCSRM throughout a wide speed range. The results are validated using commercial finite element analysis software, JMAG for electromagnetics and ACTRAN for acoustics. An acceleration test based on a setup with a 12/8 CSRM is used for experimental validation. Results show that the proposed method can provide reliable prediction of main acoustic noises during acceleration.

Index Terms—Acousitc noise, Eigen-mode, Switched reluctance machine, Synchronous reluctance machine, Vibrations.

I. INTRODUCTION

SWITCHED reluctance motors (SRMs) have been considered for years as a candidate for both electric vehicle (EV) and hybrid electric vehicle (HEV) applications due to their power density, mechanically robust design, wide constant power range, and high temperature tolerance afforded by a lack of permanent magnet materials. However, the problems of vibration and acoustic noise remain as major detriments of the SRM when compared against other potential alternatives; namely permanent magnet synchronous motors and induction motors. The mutually-coupled SRM (MCSRM) with sine-wave excitation is considered to be quieter than the conventional SRM (CSRM) [1]. However, the acoustic noise performance has not been calculated in the full speed range in literature. Efforts towards the calculation and reduction of acoustic noise in SRMs have been made in various aspects in literature. It is widely accepted that radial force between the rotor and stator is the primary source of acoustic noises in SRMs. The radial forces are commonly calculated from finite element analysis (FEA) numerical models. Some analytical

force prediction methods are also proposed to speed up the calculation [2], [3]. However, the numerical methods are time-consuming and not suitable for the design or optimization purpose where an extensively large number of candidates are evaluated; meanwhile, the analytical methods are not reliable in accuracy, especially when the drive sampling and switching effects are considered. Bösing proposed a method based on FEA calculated offline lookup tables (LUTs) to obtain the radial forces, which is with acceptable accuracy and satisfactory simulation time [4]. Similar approaches are also used for control optimization to reduce the acoustic noise [5].

Analyses of stator vibrational behavior and noise radiation are another two stages of acoustic noise calculation. Currently, numerical software packages, such as ACTRAN, are available to calculate the vibration and related sound by using either the direct frequency response method or the modal superposition method [1], [4], [6]–[9]. However, finite element based modeling and calculation of the numerical model are time-consuming, especially when the switching effects brought by the pulse width modulated (PWM) voltage source inverter are considered. Design, optimization and control require faster analytical methods. Various models are proposed in literature for analytical calculation of the natural frequencies or transmission impedance of the SRM stator and the radiation efficiency of the stator surface [2], [10]–[14]. However, most of them ignore the frame effects [15] and the switching effects on vibration behavior.

This paper derives general expressions to the spatial-temporal harmonic orders of CSRM and MCSRM; proposes a hybrid approach of acoustic noise analysis by extending Bösing's dynamic model [4] to cover the MCSRM case considering the frame effects in more details; compares the acoustic noise of CSRM and MCSRM in a wide speed range by using the proposed approach. A CSRM and an MCSRM designed for HEV applications are investigated. The motor geometry and the analysis procedure are introduced in Section II. In Section III, the air-gap radial force spatial-temporal components and the dynamic modelling are presented. The natural frequencies of the stator are evaluated considering the frame effects in Section IV. The surface displacements and radiated sound power of the stator are calculated in Section V. The analytical results are validated by numerical simulations by using ACTRAN in conjunction with JMAG in Section VI. The noise spectra of the two motors in the full speed range are then calculated and compared through the use of

waterfall diagrams. In Section VII, a 12/8 CSRM protoype with downscaled power rating is used to validate the proposed method experimentally through an acceleration test.

II. MOTOR TOPOLOGY AND ANALYSIS METHODOLOGY

A. Motor Specification

A 24/16 SRM designed for HEV application is analyzed in this paper [16]. Main parameters of the motor are listed in Table I. This motor geometry and winding specification are specially optimized for the CSRM. However, it can be easily transformed to an MCSRM by just reversing the polarity of adjacent phase coils. The winding configurations and flux line distributions of the CSRM and MCSRM when phase A is excited by $200\,A$ dc current are shown in Fig. 1. It can be obviously seen from the flux lines that the two motors have different number of fundamental air-gap magnetic field pole pairs p_0, which is 4 for the CSRM and 8 for the MCSRM.

TABLE I
MAIN PARAMETERS OF THE 24/16 SRM

Peak power [kW]	60	Corner Speed [rpm]	2000
Air-gap length [mm]	0.5	Stator outer diameter [mm]	264
Peak torque [Nm]	200	Active length [mm]	92
Frame length [mm]	155	Frame thickness [mm]	26
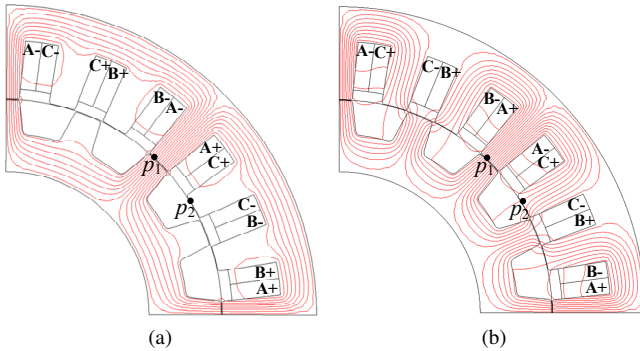
Fig. 1. Winding configurations and flux line distributions of the 24/16 SRM when phase A is excited by $200\,A$ dc current: (a) CSRM (b) MCSRM.

The CSRM is driven by an asymmetric half-bridge converter with a square-wave hysteresis current controller, as shown in Fig. 2(a); while the MCSRM is driven by a symmetric full-bridge converter with a sine-wave hysteresis current controller, as shown in Fig. 2(b). Both controllers realize the maximum
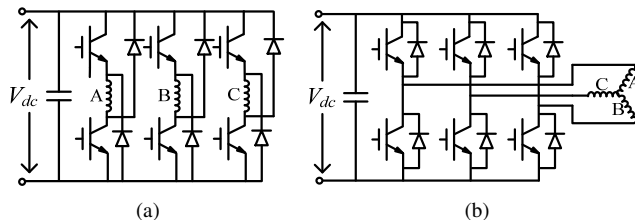
Fig. 2. Converter circuits of the SRMs: (a) CSRM (b) MCSRM.

torque per rms ampere control scheme by offline optimization.

Detailed optimization process for the CSRM is presented in [16], [17], while the optimization for the MCSRM is applied through scanning different dq current pairs. The DC-link voltage is set at $650\,V$ for the CSRM and $850\,V$ for the MCSRM, so that they have the same base speed of $2000\,rpm$. The DC-link voltage for the MCSRM is higher due to the lower power factor. The effective phase current I_{ph} is constrained to $141\,Arms$. The torque-speed curves of the two motors under the said current and voltage constraints are shown in Fig. 3, in which the contours with labels are
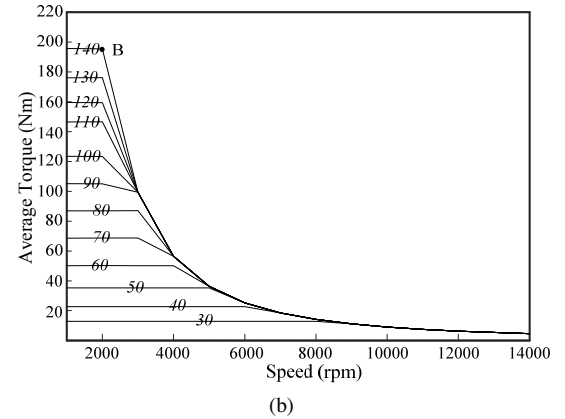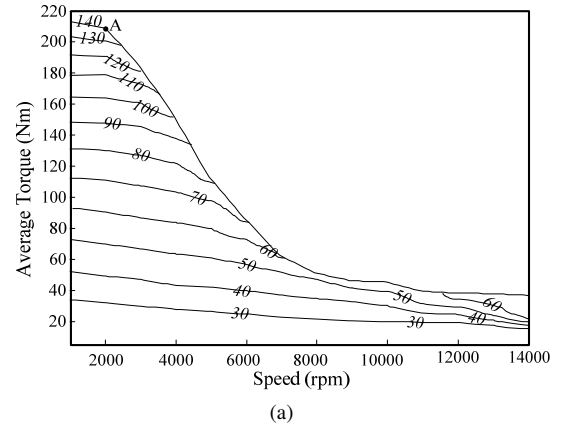
Fig. 3. Torque-speed curve of SRMs under current and voltage constraints. (a) CSRM (b) MCSRM.

effective current constraints. The torque of the MCSRM is lower than that of the CSRM, especially at high speeds, which is attributed to the facts that the motor geometry is specially optimized for the CSRM and the CSRM has a higher utilization ratio of inductance harmonics, especially when the motor is not saturated.

B. Methodology of Analysis

This paper proposes an analytical method to predict the acoustic noise of both CSRM and MCSRM. The analysis procedure is illustrated in Fig. 4. For each operation point, the resultant radial force in the air-gap is obtained from dynamic modeling, which is then decomposed into spatial-temporal harmonics. The stator natural frequency and damping ratio are analytically calculated to obtain the surface displacement from the decomposed force harmonics. Together with analytical
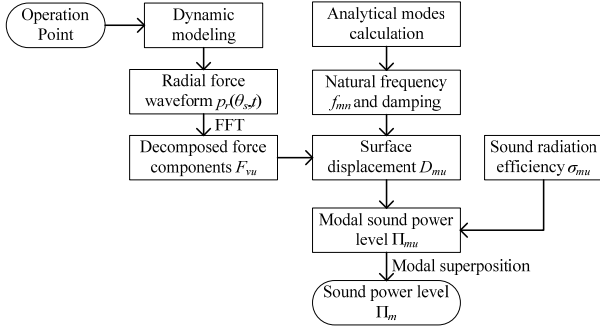
Fig. 4. Proposed acoustic noise analysis procedure

Fig. 5. Radial magnetic pressure distribution of the 24/16 motor when phase A is excited by 200 A dc current. (a) CSRM (b) MCSRM.

sound radiation efficiency results, the sound power level is evaluated through modal superposition.

III. RADIAL FORCE COMPONENTS AND DYNAMIC MODELLING

A. Radial Force Calculation and Spatial-Temporal Decomposition

The Maxwell stress tensor or the virtual work method are extensively used with FEA models to calculate the air-gap radial magnetic force per unit area, or the magnetic pressure, which is the source of electromagnetic excited acoustic noise. For the ease of noise calculation, the air-gap magnetic pressure waveform p_r as a function of stator spatial position θ_s and time t can be transformed into spatial orders and temporal harmonics by using two dimensional fast Fourier transformations (2D FFT). p_r waveform is then decomposed into its spatial-temporal harmonic series:

$$p_r(\theta_s,t) \xrightarrow{\text{2D FFT}} \sum_{v=0}^{v_{max}} \left\{ \text{Re}\left(\sum_{u=N_{nm}}^{N_{pm}} p_{vu} e^{ju\omega t + v\theta_s} \right) \right\} \quad (1)$$

where v is the spatial order, v_{max} is the maximum spatial order considered, p_{vu} is the positive-negative sequence Fourier series, u is the frequency order, and ω is the rotor angular velocity. N_{pm} and N_{nm} are the maximum positive and negative harmonic orders respectively [4].

In both CSRMs and MCSRMs with symmetric excitation, the spatial distribution of p_r is periodic according to the magnetic poles and phase pairs:

$$p_r(\theta_s,t) = p_r(\theta_s \pm \frac{2\pi}{v_{base}}, t) \quad (2)$$

where v_{base} is the spatial order related to the p_0, the number of stator slots N_s and the number of phases N_{phase}:

$$v_{base} = \gcd(\frac{N_s}{N_{phase}}, 2p_0) \quad (3)$$

By substituting (2) into (1), we can derive

$$\text{mod}(v, v_{base}) = 0, \text{ i.e. } v = \{0, v_{base}, 2v_{base}, \dots\} \quad (4)$$

Take the 24/16 motor shown in Fig. 1 as an example. Although p_0 of the MCSRM is two times more than the CSRM (8 vs. 4), v_{base} is 8 for both according to (3), which is verified by the p_r distribution presented in Fig. 5.

As is shown in Fig. 6, for both CSRM and MCSRM, two points in the air gap with a spatial distance of one stator pole pitch (see p_1 and p_2 in Fig. 1) are excited with the same force and a time difference of one stroke [18], i.e.

$$p_r(\theta_s,t) = p_r(\theta_s \pm \frac{2\pi}{N_s}, t \mp \frac{2\pi}{\omega}\frac{1}{S_f}) \quad (5)$$

where S_f is the number of force cycles per mechanical revolution. For CSRMs, S_f is the same as the number of strokes:

$$S_f = N_{phase}N_r \quad (6)$$

where N_r is the number of rotor poles. For MCSRMs, S_f is calculated as

$$S_f = 2N_{phase}p_0 \quad (7)$$

since there are $2N_{phase}$ force strokes during one electrical period. Here S_f for the CSRM and the MCSRM are both 48. By substituting (5) into (1), for a specific spatial order v, the temporal frequency order sequence u is

$$u = v\frac{S_f}{N_s} \pm nS_f, \ n = 0,1,2,\dots \quad (8)$$

If the SRM is excited by pulse width modulation (PWM) with switching frequency f_{PWM}, the force waveform will be modulated [19]. As a result, the temporal frequency order sequence is shifted and the frequency is expressed as

$$f_u = u \cdot f_{mec} + l \cdot f_{PWM}, \ l = 0 \text{ or } \pm 1 \quad (9)$$

where $f_{mec} = \omega/2\pi$ is the rotational mechanical frequency.

B. Dynamic Modelling with Radial Magnetic Pressure

An LUT-based dynamic motor model is proposed to calculate the radial magnetic pressure, as shown in Fig. 7. In order to consider the nonlinearity and harmonics, the $\psi - i$ magnetization curves of the motor are obtained by running a number of static FEA calculations with different current excitation conditions (angle and phase). The magnetization curves are then inverted to offline $i - \psi$ LUT [20]. Similar LUTs for the air-gap radial magnetic pressure distribution $p_r(\theta_s)$ and co-energy torque T_{co} are also generated. For the CSRM, the LUTs and motor dynamic model are built in
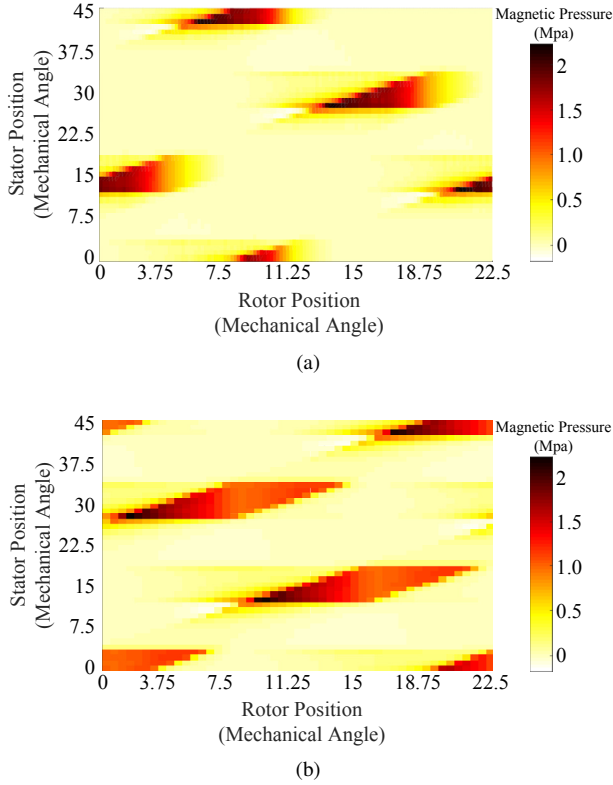
Fig. 6. 1/8 of air-gap magnetic pressure spatial-temporal distributions during one rotor pitch in the 24/16 SRM with $n = 2000\,\mathrm{rpm}$, $I_{ph} = 141$ Arms. (a) CSRM (b) MCSRM.

the stator reference system and it is assumed that there is no mutual coupling (a spatial-based, per-phase model). For the MCSRMs, they are built in the synchronous rotating dq reference system considering spatial harmonics [4], [21]. The LUTs are evaluated for each spatial harmonics and composed in the frequency domain.

The motor models and corresponding controller models are implemented in MATLAB/Simulink. Motor current waveforms under various working conditions can be simulated considering the switching, control parameters, magnetic nonlinearity, and spatial harmonics. Then the magnetic pressure waveforms $p_r(\theta_s, t)$ are obtained from the LUTs through interpolation.

IV. VIBRATION MODES CONSIDERING FRAME EFFECTS

A. Stator Core with Windings

Motor stator cores are commonly treated as infinite length cylindrical shells since they are usually free in the axial direction while the teeth and coils are considered to be additional masses for analytical modal analysis [22]–[24]. The natural frequency of the stator core of the $m-$th circumferential vibration mode is solved as

$$f_m = \frac{1}{2\pi}\sqrt{\frac{K_m^c}{M_m^c + M_m^t}} \tag{10}$$

where K_m^c and M_m^c are the lumped stiffness and mass of the stator yoke; M_m^t is the lumped mass of the teeth and coils
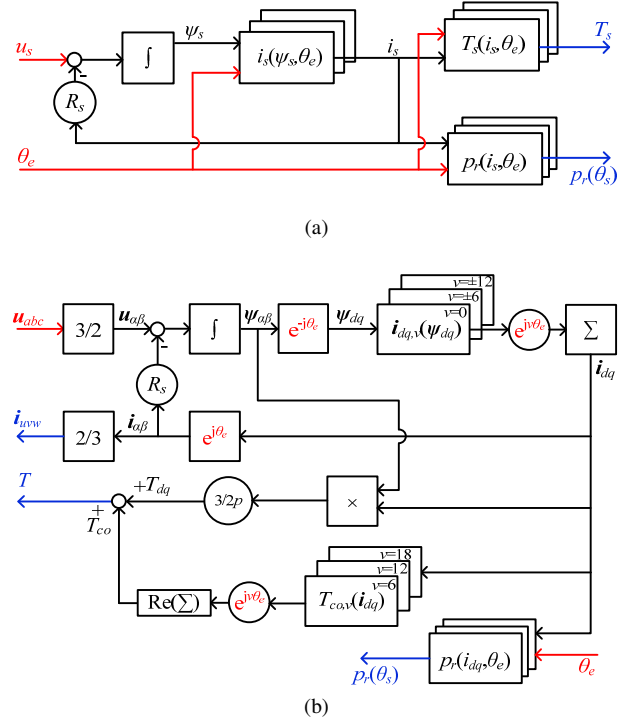
Fig. 7. Dynamic motor models of the SRM with magnetic pressure LUTs: (a) CSRM (b) MCSRM.

region, including laminations, conductors and insulation. K_m^c is solved from (11)

$$K_m^c = \frac{4\Omega_m^2}{D_c}\frac{\pi L_{stk}h_c E_c}{1 - v_c^2} \tag{11}$$

where E_c and v_c are the elasticity modulus and Poissons ratio of the stator laminations respectively; h_c, D_c, and L_{stk} are the thickness, mean diameter and stack length of the stator yoke respectively; Ω_m is the non-dimensional frequency which is the root of the characteristic equation of motion of the cylindrical shells:

$$\begin{cases} \Omega_0^2 = 1, & \text{for } m = 0 \\ \Omega_m^2 = \frac{1}{2}[1 + m^2 + \kappa m^4] \mp \\ \quad \frac{1}{2}\sqrt{[1 + m^2 + \kappa m^4]^2 - 4\kappa m^6}, & \text{for } m \geq 1 \end{cases} \tag{12}$$

where $\kappa = \frac{h_c}{\sqrt{3}D_c}$ is a non-dimensional parameter.

B. Frame Effect

The stator frame can be simplified as a thin cylindrical shell with both ends constrained by the simply supported conditions. The cooling ribs and fins are treated as additional masses. The lumped stiffness of the frame of $m-$th circumferential mode and $n-$th axial mode then is calculated as

$$K_{mn}^f = \frac{4\Omega_{mn}^2}{D_f}\frac{\pi L_f h_f E_f}{1 - v_f^2} \tag{13}$$

where E_f and v_f are the elasticity modulus and Poissons ratio of the stator laminations respectively; h_f, D_f, and L_f are the

thickness, mean diameter and length of the frame respectively. Ω_{mn} is solved from the characteristic equation

$$\Omega_{mn}^6 - K_2\Omega_{mn}^4 + K_1\Omega_{mn}^2 - K_0 = 0 \tag{14}$$

The coefficients K_0-K_2 in (14) are defined according to the Donnel-Mushtari theory and given in [22].

Since both the stator core and the frame are considered as cylindrical shells, the stator-frame system can be considered as a multi-layer coaxial cylindrical shell. The resultant lumped stiffness and mass are calculated from those of each layer [15]:

$$\begin{cases} K_{mn}^s = K_m^c + K_m^t + \lambda_f K_{mn}^f \\ M_{mn}^s = \lambda_m(M_m^c + M_m^t + M_{mn}^f) \end{cases} \tag{15}$$

where λ_f and λ_m are factors to consider the thickness of the frame and can be obtained through the following:

$$\lambda_f = \frac{D_f h_{ef}}{D_{ef} h_f}, \quad D_{ef} = \frac{D_f + D_c}{2}, \quad h_{ef} = h_f + h_c$$

$$\lambda_m = \begin{cases} 1, & m = 0 \\ \dfrac{m^2 + 1}{m^2}, & m \geq 1 \end{cases} \tag{16}$$

Then the natural frequency of each vibration mode is calculated as

$$f_{mn} = \frac{1}{2\pi}\sqrt{\frac{K_{mn}^s}{M_{mn}^s}}. \tag{17}$$

V. Sound Power Estimation

For the $m-$th circumferential mode, only the force component with the same spatial order ($v = m$) can excite significant vibration and acoustic noise. The resulting displacement amplitude D_{mu} is calculated as

$$D_{mu} = \frac{F_{vu}/M_{mn}^s}{\sqrt{(\omega_m^2 - \omega_{vu}^2)^2 + 4\zeta_m^2\omega_{vu}^2\omega_m^2}} \tag{18}$$

where F_{vu} is the force amplitude and calculated as $F_{vu} = \pi D_{si}L_{stk}p_{vu}$, D_{si} is the stator inner diameter. $\omega_m = 2\pi f_m$ is the angular natural frequency of the circumferential mode m, and D_{si} is the angular frequency of the force component with spatial order v and temporal frequency order u. ζ_m is the modal damping ratio of mode m, which should be measured through experiments. An expression of ζ_m obtained from empirical fit of experiments on different motors is given in [25].

The sound radiation can be analyzed by calculating the sound power in the frequency domain for each vibration mode m and then superimposing the results of each of the vibration modes [26]. The modal sound power of frequency component u radiated from the frame surface Π_{mu} is

$$\Pi_{mu} = \sigma_m \rho_0 c_0 S \omega_{vu} D_{mu} \tag{19}$$

where ρ_0 and c_0 are the mass density of the air and the speed of sound in air, respectively. S is the area of the sound radiation surface. σ_m is the modal radiation efficiency, which is a function of vibration frequency. Here finite length cylindrical shell model is used due to the fact that both ends of the frame

are supported. The analytical expression of σ_m for the finite length cylindrical shell is derived in [27].

$$\sigma_m(\omega_e) = \int_{-k_0}^{k_0} \frac{2k_0 l}{\pi^2 a k_r^2 \left| \frac{\mathrm{d}H_m^{(2)}(k_r a)}{\mathrm{d}(k_r a)} \right|^2} \left[\frac{\pi/l}{k_z + \pi/l} \right]^2 \cdot \frac{\sin^2[(k_z - \pi/l)l/2]}{[(k_z - \pi/l)l/2]^2} \mathrm{d}k_z \tag{20}$$

where k_0 is the acoustic waveform number, which is related to the excitation frequency of vibration ω_e by $k_0 = \omega_e/c_0$. k_r and k_z are the radial and axial components of the acoustic wave number respectively, and they are related by $k_0^2 = k_z^2 + k_r^2$. The sound radiation efficiency of the 24/16 SRM calculated from (20) is shown in Fig. 8. It is obvious that the sound radiation efficiency of mode $m = 0$ reaches unity much faster than the higher modes, which means that it can contribute to significant noise at low frequencies.
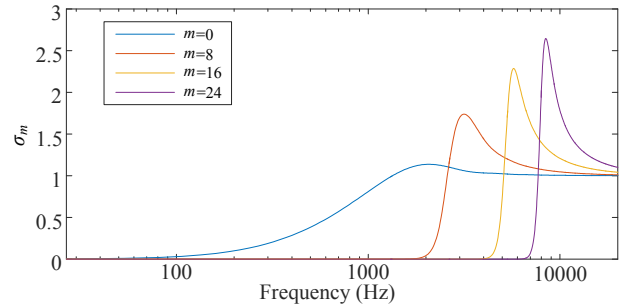
Fig. 8. Sound radiation efficiency of different modes for the 24/16 SRM.

VI. Numerical Validation

A. Radial Force Calculation

Fig. 9 presents the simulated current waveforms of the two motors obtained from the dynamic simulation models shown in Fig. 7, when they are operated at the corner speed $n = 2000\,\mathrm{rpm}$ (point A and B in Fig. 1). The air-gap radial magnetic pressure waveforms are also obtained from the results of current waveforms after the simulation reaches steady state. Corresponding temporal-spatial spectra are presented in Fig. 10. Obviously, force components with spatial harmonic orders of 0, 8, 16 and 24 are dominant. For each said spatial harmonic, the significant temporal harmonic orders are offset by 48, which conforms to the prediction of (4) and (8). For each spatial harmonic, the higher the temporal order is, the lower the amplitude.

B. Vibration and Noise Results Validation

Structural-acoustic numerical simulation models are built in acoustic analysis software ACTRAN to validate the proposed analytical approach. The nodal force on the stator surface calculated using JMAG is exported as loads to the structural model built in ACTRAN. The structural model and simulated vibrational mode shapes are presented in Fig. 11 while corresponding natural frequencies are compared with the analytical ones in Table II. The maximum divergence of the analytical result related to the numerical result is within 20%.
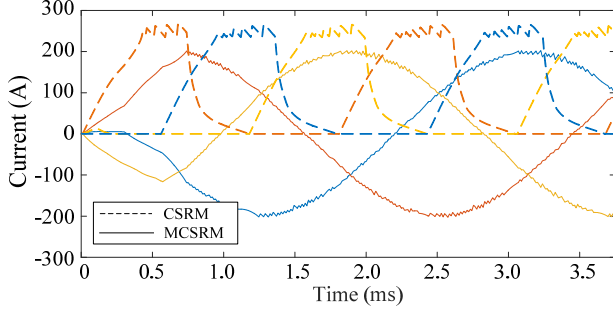
Fig. 9. Transient current waveforms of CSRM and MCSRM obtained from the dynamic models.
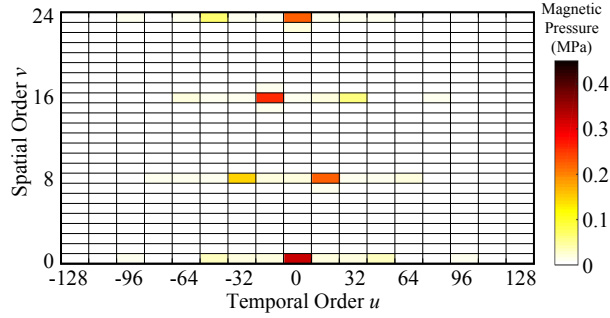
(a)
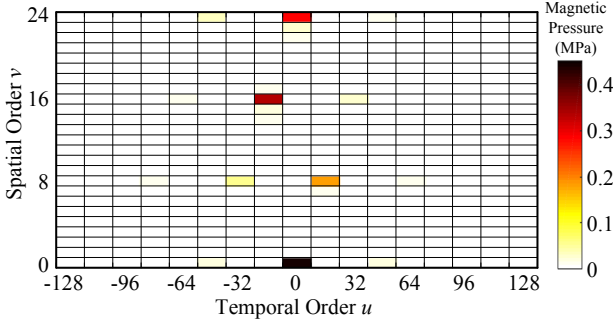
(b)

Fig. 10. Temporal-spatial spectrum of the 24/16 SRM when $n = 2000\,\mathrm{rpm}$, $I_{ph} = 141\,\mathrm{Arms}$: (a) CSRM (b) MCSRM.
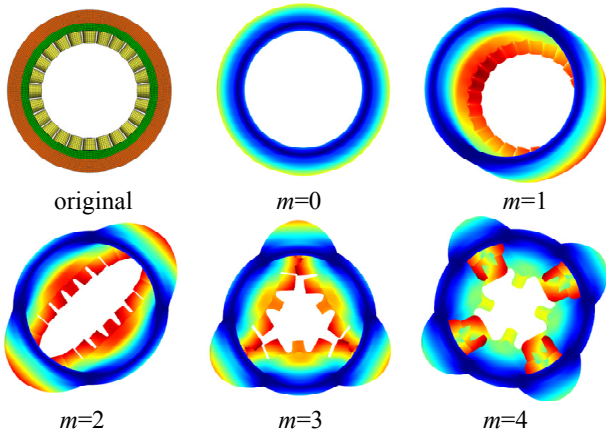
Fig. 11. Plane view of structural model and first 5 vibration modes obtained from ACTRAN.

TABLE II
COMPARISON OF NATURAL FREQUENCY RESULTS

	$m = 0$	$m = 1$	$m = 2$	$m = 3$	$m = 4$
ACTRAN [Hz]	5316	3680	2996	3831	5340
Analytical [Hz]	5452	4303	3324	4031	5494

The numerically simulated instantaneous displacement distribution of the stator and sound pressure distribution around the motor are presented in Fig. 12. Mode $m = 0$ can be clearly observed as the main contributor to the stator deformation and the sound pressure. Fig. 13 compares the spatial averaged
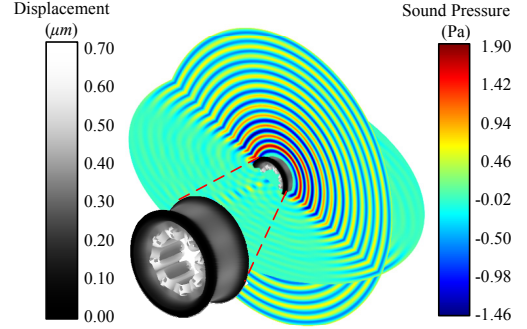
Fig. 12. Numerical simulated results of the 24/16 CSRM at $t = 0.0026\,\mathrm{s}$ when $n = 2000\,\mathrm{rpm}$.

sound pressure level (SPL) spectra at a sphere surface, which is one meter away from the motor surface. SPL spectra are calculated by the analytical method and the numerical method. The numerical results are obtained by integral averaging of the sound pressure at the sphere surface, and the analytical results are obtained from the modal superimposed sound power level, SWL:

$$\mathrm{SPL} = \mathrm{SWL} - 10\log_{10}\left(\frac{4\pi r_d^2}{S_0}\right) \qquad (21)$$

where $r_d = 1.0 + 0.5L_{max}$ [m] (L_{max} is the maximum linear dimension of the motor in meters), and $S_0 = 1\,\mathrm{m}^2$ [28]. The results for both motors show a satisfactory overall agreement between the analytically-calculated spectra and the numerically calculated ones, both in shape and amplitude. However, there are some large differences around $5000\,\mathrm{Hz}$, caused by the divergence of natural frequencies and sound radiation efficiency. The most significant SPLs occur at $1600\,\mathrm{Hz}$, which is mainly due to the harmonic pair $u = \pm 48$ and $v = 0$.

C. CSRM vs. MCSRM Excitation

By applying the proposed analytical approach to the operation points along the outermost torque-speed curves in Fig. 3, the SPL waterfall diagrams are calculated when the two motors are accelerated from $n = 0\,\mathrm{rpm}$ to $14\,000\,\mathrm{rpm}$ as shown in Fig. 14.

The effect of $1600\,\mathrm{Hz}$ with $u = \pm 48$ temporal radial harmonic with spatial order $v = 0$ is apparently visible in the waterfall diagrams. Although the $u = \pm 16$ temporal radial force harmonics with spatial order $v = 8$ and $v = 16$ are much higher than $u = \pm 48$, they produce much lower SPL results because the natural frequency and damping ratio of $m = 8$ and
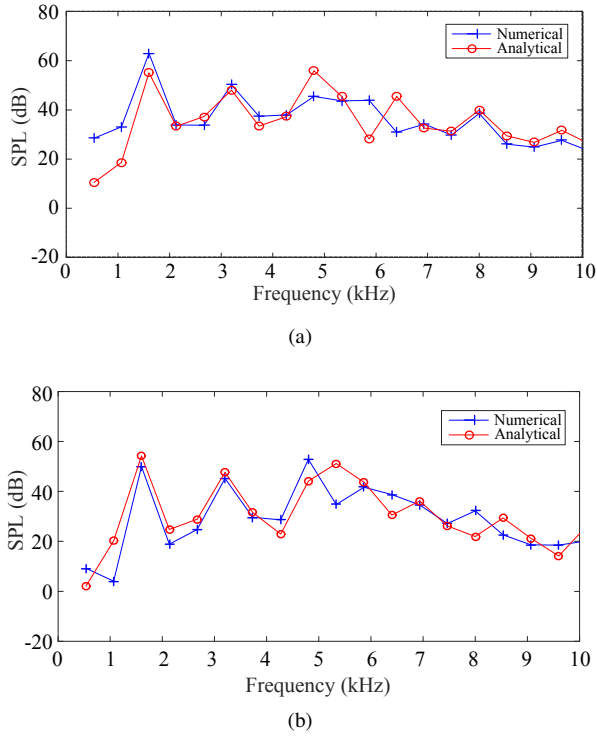
Fig. 13. SPL spectra calculated by the proposed method and numerical model when n=2000 rpm: (a) CSRM (b) MCSRM.
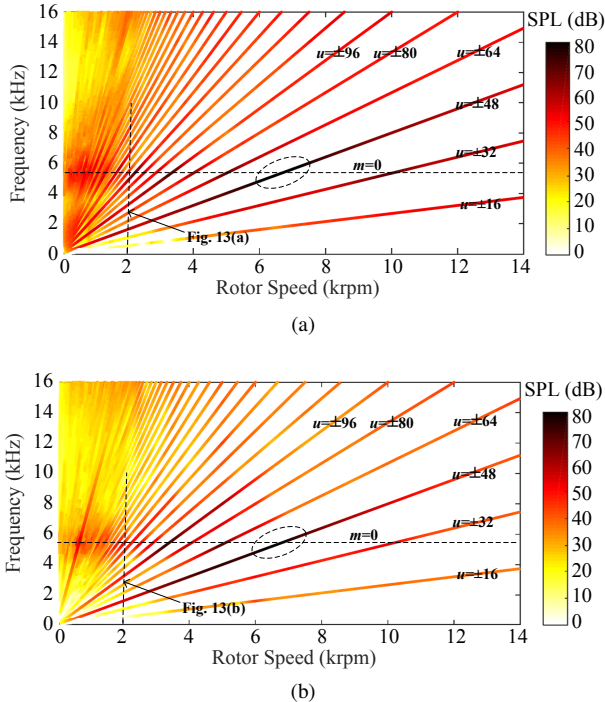
Fig. 14. Waterfall diagrams of SPL results calculated by the proposed method: (a) CSRM (b) MCSRM.

16 are too high to produce significant vibrations according to (18), while the radiation efficiency is lower in the considered frequency range (see Fig. 8). For different rotor speeds, the most noisy regions lie around the natural frequency of $m = 0$, as indicated by the horizontal lines drawn in Fig. 14.

Resonance between the $m = 0$ mode and the $u = \pm48$ (3 times the fundamental frequency of the absolute current waveform) force components occur from $6000\,\text{rpm}$ to $8000\,\text{rpm}$, which results in highest noise over the whole speed region, as indicated by the dashed ellipses in Fig. 14. Similar phenomena are also observed through experiments in [5], [29], [30]. There are also some noisy regions at the frequency of $14\,\text{kHz}$ or higher, especially with low rotor speeds, which can be attributed to switching effects.

The air-gap radial magnetic force strokes of the MCSRM have a longer period than those of the CSRM, which results from the use of continuous phase currents. The continuous phase currents also contribute to higher amplitudes of the low order harmonics in the force waveform, which is shown in Fig. 10. However, for high order force harmonics, the amplitudes of the MCSRM are lower. Since the acoustic noises are mainly contributed by temporal harmonics 48th or higher, the SPLs of the MCSRM are lower than the CSRM, especially in low speed regions, as presented in Fig. 14.

VII. Experiment and Results Investigation

Since the prototype and test setup of the 24/16 motor are not available, a 12/8 CSRM prototype with downscaled power rating is used for experimental validation. Main parameters of the 12/8 CSRM are listed in Table III.

TABLE III
MAIN PARAMETERS OF THE 12/8 CSRM PROTOTYPE.

Rated Power [kW]	2	Rated Speed [rpm]	6000
Air-gap length [mm]	0.3	Stator outer diameter [mm]	136
Active length [mm]	70	Stator teeth height [mm]	14.9

The setup to measure the noise of the prototype is shown in Fig. 15. Noise emitted from the prototype is measured by condenser microphones pointing to the prototype at different positions. The measured signals are captured by a professional audio interface with a sampling frequency of 192 kHz before sending to the laptop for data processing and visualization. Motor speed and current are also sent to the laptop simultaneously through the motor controller. Motor drive and controller implementation is the same as presented in [31] except that the hysteresis current controller is used.

An acceleration test from $0\,\text{rpm}$ to $6000\,\text{rpm}$ in $2\,\text{s}$ is carried out to obtain the noise spectra of the prototype. To avoid the interference of the load motor, the shaft coupling to the load is detached during acceleration. The reference current in the motor controller is fixed to be $5\,\text{A}$ to achieve a nearly constant acceleration rate. The noise during the acceleration is first calculated by the proposed method with the same drive settings. Calculated natural frequencies of mode $m = 0$ and $m = 4$ are $10\,078\,\text{Hz}$ and $8175\,\text{Hz}$ respectively. The calculated waterfall diagram of the spatial averaged SPL is
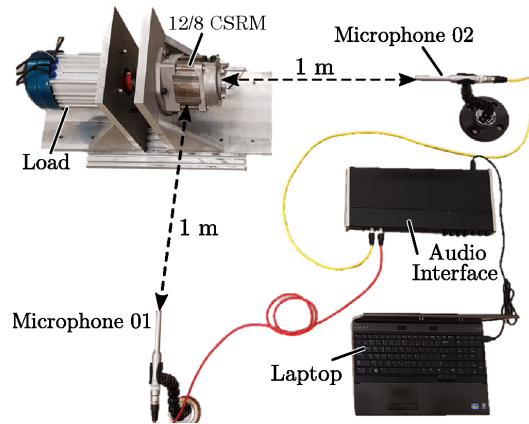
Fig. 15. Noise measurement setup of the 12/8 CSRM.
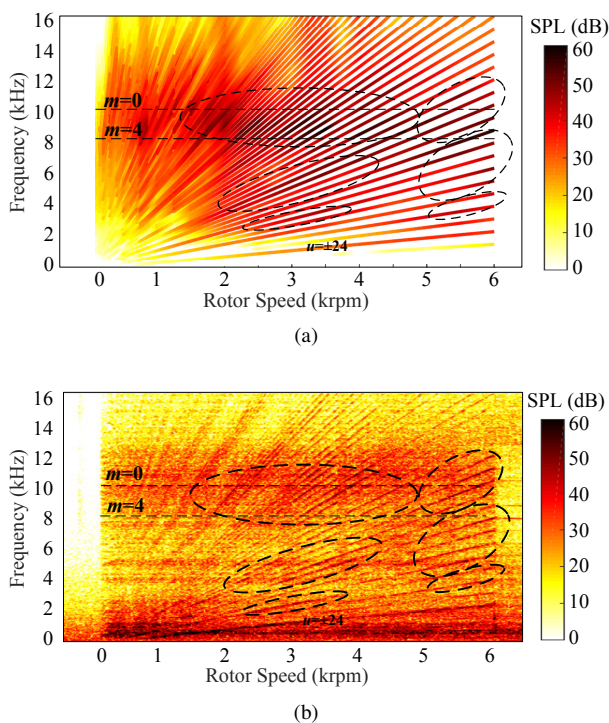
Fig. 16. SPL waterfall diagram of the 12/8 CSRM when accelerated by 5 A currents: (a) calculated result (b) experimental result.

shown in Fig. 16(a), while the measured result by Microphone 01 in Fig. 15 is shown in Fig. 16(b).

Apparently, the measured noise is much more significant than the calculated result in the low frequency region, which is contributed by the aerodynamic, mechanical vibration of the setup and background noise emitted from dc power source and other equipment in the lab. The large difference exists between the calculated and measured results here is mainly due to those factors are not considered in our calculation. Apart from the low frequency region, we can see that both the calculated result and the measured result indicate that the most noisy region lies around $8\,\mathrm{kHz}$ and $10\,\mathrm{kHz}$, as is marked by horizontal dashed lines in Fig. 16, which is consistent with the calculated natural frequencies of mode $m = 0$ and $m = 4$.

As shown in Fig. 16(a) and (b), the first significant noise

harmonic predicted by the proposed method is $u = \pm24$, which is 3 times of fundamental electrical frequency. The first non-aerodynamic noise harmonic order measured is the same. Except from the aerodynamic noise and background noise, the most noisy regions predicted by the calculation overlap well with those obtained from measurement, as illustrated by the dashed ellipses in Fig. 16. There are certain differences between the amplitudes of calculated and measured SPLs, which are caused by many factors: the calculation gives the spatial averaged result while the experiment measures the noise at a particular point, which are also observed in [32]; the calculation does not consider all the harmonics and there are differences between the empirically obtained modal damping ratio and the real ones.

VIII. CONCLUSION

A hybrid method to predict the acoustic noise for both CSRM and MCSRM considering frame effects has been presented in the paper. Analytical expressions to stator radial force spatial and temporal harmonic orders are presented. The proposed method can be used for fast prediction of a CSRM or an MCSRMs acoustic noise spectrum throughout a wide operating region, which is of particular importance when the motor noise performance has to be assessed under various operating points. After applying the method to a CSRM and MCSRM with the same geometry in their full speed ranges, it has been observed that the MCSRM emits less noise than the CSRM, especially at low speeds. However, the MCSRM does produce less torque especially at high speeds due to the fact that the motor geometry is specially optimized for the CSRM.

A 12/8 CSRM prototype is used for experimental validation of the proposed method. Reults show that the proposed method is able to predict the main non-aerodynamic noises favorably as compared to acceleration test. Both the calculated results and the measured results show that the interaction between mode $m = 0$ and the force components with 3 times frequency of the absoluted current waveform plays a significant role in acoustic noise of SRMs. More comprehensive experiments would be involved as future works for further validation and improvement of the proposed calculation method.

REFERENCES

[1] X. Liang, G. Li, J. Ojeda, M. Gabsi, and Z. Ren, "Comparative study of classical and mutually coupled switched reluctance motors using multiphysics finite-element modeling," *IEEE Trans. Ind. Electron.*, vol. 61, no. 9, pp. 5066–5074, Sep. 2014.
[2] M. Anwar and I. Husain, "Radial force calculation and acoustic noise prediction in switched reluctance machines," *IEEE Trans. Ind. Appl.*, vol. 36, no. 6, pp. 1589–1597, Nov. 2000.

[3] J. O. Fiedler and R. W. D. Doncker, "Simplified calculation of radial force spectrum in SRM for acoustic noise prediction in preliminary machine design," in *The 3rd IET International Conference on Power Electronics, Machines and Drives, 2006*, Apr. 2006, pp. 652–656.

[4] M. Bösing, "Acoustic modeling of electrical drives," PhD Dissertation, RWTH Aachen University, Aachen, Germany, May 2014.

[5] J. Bayless, N. Kurihara, H. Sugimoto, and A. Chiba, "Acoustic noise reduction of switched reluctance motor with reduced RMS current and enhanced efficiency," *IEEE Trans. Energy Convers.*, vol. 31, no. 2, pp. 627–636, Jun. 2016.

[6] C. Lin and B. Fahimi, "Prediction of acoustic noise in switched reluctance motor drives," *IEEE Trans. Energy Convers.*, vol. 29, no. 1, pp. 250–258, Mar. 2014.

[7] J. Li and Y. Cho, "Investigation into reduction of vibration and acoustic noise in switched reluctance motors in radial force excitation and frame transfer function aspects," *IEEE Trans. Magn.*, vol. 45, no. 10, pp. 4664–4667, Oct. 2009.

[8] M. van der Giet, E. Lange, D. A. P. Correa, I. E. Chabu, S. I. Nabeta, and K. Hameyer, "Acoustic simulation of a special switched reluctance drive by means of field-circuit coupling and multiphysics simulation," *IEEE Trans. Ind. Electron.*, vol. 57, no. 9, pp. 2946–2953, Sep. 2010.

[9] F. L. M. dos Santos, J. Anthonis, F. Naclerio, J. J. C. Gyselinck, H. van der Auweraer, and L. C. S. Góes, "Multiphysics NVH modeling: simulation of a switched reluctance motor for an electric vehicle," *IEEE Trans. Ind. Electron.*, vol. 61, no. 1, pp. 469–476, Jan. 2014.

[10] W. Finley, M. Hodowanec, and W. Holter, "An analytical approach to solving motor vibration problems," *IEEE Trans. Ind. Appl.*, vol. 36, no. 5, pp. 1467–1480, Sep. 2000.

[11] W. Cai and P. Pillay, "Resonant frequencies and mode shapes of switched reluctance motors," *IEEE Trans. Energy Convers.*, vol. 16, no. 1, pp. 43–48, Mar. 2001.

[12] D. E. Cameron, J. H. Lang, and S. D. Umans, "The origin and reduction of acoustic noise in doubly salient variable-reluctance motors," *IEEE Trans. Ind. Appl.*, vol. 28, no. 6, pp. 1250–1255, Nov. 1992.

[13] J. P. Lecointe, R. Romary, J. F. Brudny, and M. McClelland, "Analysis and active reduction of vibration and acoustic noise in the switched reluctance motor," *IEE Proceedings - Electric Power Applications*, vol. 151, no. 6, pp. 725–733, Nov. 2004.

[14] Z. Q. Zhu, X. Liu, and Z. Pan, "Analytical model for predicting maximum reduction levels of vibration and noise in switched reluctance machine by active vibration cancellation," *IEEE Trans. Energy Convers.*, vol. 26, no. 1, pp. 36–45, Mar. 2011.

[15] S. M. Castano, B. Bilgin, E. Fairall, and A. Emadi, "Acoustic noise analysis of a high-speed high-power switched reluctance machine: frame effects," *IEEE Trans. Energy Convers.*, vol. 31, no. 1, pp. 69–77, Mar. 2016.

[16] W. Jiang, "Three-phase 24/16 switched reluctance machine for hybrid electric powertrains: design and optimization," Thesis, 2016. [Online]. Available: http://macsphere.mcmaster.ca/handle/11375/19087

[17] J. W. Jiang, B. Bilgin, B. Howey, and A. Emadi, "Design optimization of switched reluctance machine using genetic algorithm," in *2015 IEEE International Electric Machines Drives Conference (IEMDC)*, May 2015, pp. 1671–1677.

[18] L. Vandevelde, J. J. Gyselinck, F. Bokose, and J. A. Melkebeek, "Vibrations of magnetic origin of switched reluctance motors," *COMPEL - The international journal for computation and mathematics in electrical and electronic engineering*, vol. 22, no. 4, pp. 1009–1020, Dec. 2003. [Online]. Available: http://www.emeraldinsight.com/doi/abs/10.1108/03321640310482968

[19] A. Hofmann, M. Harries, E. Weienborn, and R. W. D. Doncker, "Making the acoustic case for hysteresis control in switched reluctance machines," in *7th IET International Conference on Power Electronics, Machines and Drives (PEMD 2014)*, Apr. 2014, pp. 1–6.

[20] J. R. Hendershot and T. J. E. Miller, *Design of Brushless Permanent-Magnet Machines*, 2nd ed. Venice, FL USA: Motor Design Books LLC, Mar. 2010.

[21] N. Bianchi and L. Alberti, "MMF harmonics effect on the embedded FE analytical computation of PM motors," *IEEE Trans. Ind. Appl.*, vol. 46, no. 2, pp. 812–820, Mar. 2010.

[22] A. W. Leissa, "Vibration of Shells," NASA, Washington, D.C., USA, Technical Report NASA SP-288, Jan. 1973. [Online]. Available: http://ntrs.nasa.gov/search.jsp?R=19730018197

[23] J. F. Gieras, *Noise of Polyphase Electric Motors*. Boca Raton, FL: CRC Press, Dec. 2005.

[24] S. Huang, M. Aydin, and T. Lipo, "Electromagnetic vibration and noise assessment for surface mounted PM machines," in *Power Engineering Society Summer Meeting, 2001*, vol. 3, Jul. 2001, pp. 1417–1426 vol.3.

[25] S. J. Yang, *Low-Noise Electrical Motors*. Oxford University Press, Jan. 1981.

[26] J. Fiedler, K. Kasper, and R. De Doncker, "Calculation of the acoustic noise spectrum of SRM using modal superposition," *IEEE Trans. Ind. Electron.*, vol. 57, no. 9, pp. 2939–2945, Sep. 2010.

[27] C. Wang and J. Lai, "The sound radiation efficiency of finite length circular cylindrical shells under mechanical excitation II: limitations of the infinite length model," *J. Sound Vib.*, vol. 241, no. 5, pp. 825–838, Apr. 2001. [Online]. Available: http://linkinghub.elsevier.com/retrieve/pii/S0022460X00933388

[28] *Motors and Generators*. National Electrical Manufacturers Association, MG 1-2009, 2009.

[29] M. Takiguchi, H. Sugimoto, N. Kurihara, and A. Chiba, "Acoustic Noise and Vibration Reduction of SRM by Elimination of Third Harmonic Component in Sum of Radial Forces," *IEEE Trans. Energy Convers.*, vol. 30, no. 3, pp. 883–891, Sep. 2015.

[30] A. Hofmann, A. Al-Dajani, M. Bsing, and R. W. D. Doncker, "Direct instantaneous force control: A method to eliminate mode-0-borne noise in switched reluctance machines," in *Electric Machines Drives Conference (IEMDC), 2013 IEEE International*, May 2013, pp. 1009–1016.

[31] F. Peng, J. Ye, and A. Emadi, "A digital PWM current controller for switched reluctance motor drives," *IEEE Transactions on Power Electronics*, vol. 31, no. 10, pp. 7087–7098, Oct. 2016.

[32] J. L. Besnerais, V. Lanfranchi, M. Hecquet, P. Brochet, and G. Friedrich, "Prediction of audible magnetic noise radiated by adjustable-speed drive induction machines," *IEEE Transactions on Industry Applications*, vol. 46, no. 4, pp. 1367–1373, Jul. 2010.
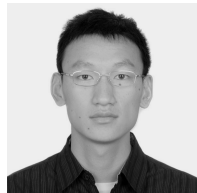
Jianning Dong (IEEE S'10-M'17) received the B.S. and Ph.D. degrees in electrical engineering from Southeast University, Nanjing, China, in 2010 and 2015, respectively. He is an Assistant Professor at the Delft University of Technology since 2016. Before joining TU Delft, he was a post-doc researcher at McMaster Automotive Resource Centre (MARC), McMaster University, Hamilton, Ontario, Canada. His main research interests are design, modelling and control of electromechanical systems.
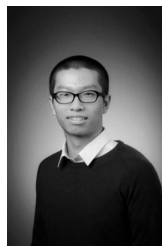
James Weisheng Jiang (IEEE S'12-M'16) received his Bachelor' Degree in vehicle engineering from College of Automotive Engineering, Jilin University, China, in 2009. He worked as a research assistant at the Clean Energy Automotive Engineering Research Center, Tongji University, China, from 2009 to 2011. He received his Ph.D. in Mechanical Engineering from McMaster University in April 2016. Currently, he is working as a Principal Research Engineer in the Program of the Canada Excellence Research Chair in Hybrid Powertrain at McMaster Automotive Resource Centre (MARC). His main research interests include design of electric vehicle and hybrid electric vehicle powertrains, design of interior permanent magnet motor, design and control of switched reluctance motor, noise and vibration analysis of traction motors.

Berker Bilgin (IEEE S'09-M12-SM16) is the Research Program Manager in Canada Excellence Research Chair in Hybrid Powertrain Program in McMaster Institute for Automotive Research and Technology (MacAUTO) at McMaster University, Hamilton, Ontario, Canada. He received his Ph.D. degree in Electrical Engineering from Illinois Institute of Technology in Chicago, Illinois, USA. He is managing many multidisciplinary projects on the design of electric machines, power electronics, electric motor drives, and electrified powertrains. Dr. Bilgin was the General Chair of the 2016 IEEE Transportation Electrification Conference and Expo (ITEC'16). He is now pursuing his MBA degree in DeGroote School of Business at McMaster University.

Alan Callegaro (IEEE S'15) received the B.S and M.S degrees in electrical engineering from Federal University of Santa Catarina (UFSC), Florianopolis, Brazil in 2011 and 2013, respectively. He worked at the Power Electronics Institute (INEP) , Florianopolis, Brazil, from 2013 to 2014. In 2015 he joined the McMaster Automotive Resource Centre (MARC) at McMaster University, Hamilton, Canada, where he is currently working toward the PhD degree in electrical engineering at the Canada Excellence Research Chair in Hybrid Powertrain Program. His research interests include high-power inverters, switched reluctance machines, noise and vibration analysis of traction motors and motor control.

Ali Emadi (IEEE S'98-M'00-SM'03-F'13) received the B.S. and M.S. degrees in electrical engineering with highest distinction from Sharif University of Technology, Tehran, Iran, in 1995 and 1997, respectively, and the Ph.D. degree in electrical engineering from Texas A&M University, College Station, TX, USA, in 2000. He is the Canada Excellence Research Chair in Hybrid Powertrain at McMaster University in Hamilton, Ontario, Canada. Before joining McMaster University, Dr. Emadi was the Harris Perlstein Endowed Chair Professor of Engineering and Director of the Electric Power and Power Electronics Center and Grainger Laboratories at Illinois Institute of Technology (IIT) in Chicago, Illinois, USA, where he established research and teaching facilities as well as courses in power electronics, motor drives, and vehicular power systems. He was the Founder, Chairman, and President of Hybrid Electric Vehicle Technologies, Inc. (HEVT) – a university spin-off company of IIT. Dr. Emadi has been the recipient of numerous awards and recognitions. He was the advisor for the Formula Hybrid Teams at IIT and McMaster University, which won the GM Best Engineered Hybrid System Award at the 2010, 2013, and 2015 competitions. He is the principal author/coauthor of over 350 journal and conference papers as well as several books including *Vehicular Electric Power Systems* (2003), *Energy Efficient Electric Motors* (2004), *Uninterruptible Power Supplies and Active Filters* (2004), *Modern Electric, Hybrid Electric, and Fuel Cell Vehicles* (2nd ed, 2009), and *Integrated Power Electronic Converters and Digital Control* (2009). He is also the editor of the *Handbook of Automotive Power Electronics and Motor Drives* (2005) and *Advanced Electric Drive Vehicles* (2014). Dr. Emadi was the Inaugural General Chair of the 2012 IEEE Transportation Electrification Conference and Expo (ITEC) and has chaired several IEEE and SAE conferences in the areas of vehicle power and propulsion. He is the founding Editor-in-Chief of the *IEEE Transactions on Transportation Electrification*.